Semicond. Sci. Technol. **21** (2006) 267–272 doi:10.1088/0268-1242/21/3/009

MBE-grown high-efficiency GaInAsSb mid-infrared detectors operating under back illumination

M H M Reddy, J T Olesberg, C Cao and J P Prineas

Optical Science and Technology Center & Department of Physics and Astronomy, University of Iowa, 205 N. Madison St, Iowa City, IA 52246, USA

E-mail: john-prineas@uiowa.edu

Received 27 July 2005, in final form 3 January 2006
Published 20 January 2006
Online at stacks.iop.org/SST/21/267

Abstract
This paper describes molecular beam epitaxial growth, processing and room temperature characterization of lattice-matched GaInAsSb mid-infrared detectors on GaSb substrates for room temperature operation. For the first time, we demonstrate GaInAsSb detectors operating under back-illumination, a critically important geometry for flip-chip-mounted focal plane arrays, and achieve performance equal or superior to front-illuminated detectors. Very high quantum efficiency and flat spectral response are achieved for the back-illuminated detectors due to improved carrier collection efficiency, photon recycling and reduced carrier recombination. *In situ* RHEED intensity oscillations and post-growth XRD are used for coarse and fine tuning of GaInAsSb lattice matching, respectively.

1. Introduction

There is much interest in 2.0–2.5 μm detectors for diverse applications in environmental and medical sensing, and astronomy. For example, we are interested in the continuous monitoring of glucose levels in blood using optical absorption spectroscopy in this wavelength range [1]. III–V semiconductor alloy materials, such as GaInAsSb/GaSb, InGaAs/InP [2], InGaSb/GaSb [3] and InGaPSb/InAs [4], have been tested so far for this wavelength region. Among these, GaInAsSb and InGaAs detectors showed the best performance. The excess strain incorporation in InGaAs detectors, which is necessary to extend its wavelength response beyond 1.71 μm, may severely limit its usefulness in the wavelength range beyond 2 μm. The GaInAsSb alloy, on the other hand, is a promising mid-infrared optoelectronic material due to the fact that the alloy can be kept lattice-matched to GaSb substrates while the energy bandgap is varied between 0.496 and 0.62 eV (2.5–2.0 μm). Many methods, such as LPE [5], MOCVD [6], OMVPE [7] and MBE [8], have been tried for the growth of the GaInAsSb/GaSb detector structures. MBE, by virtue of being a non-equilibrium growth technique and allowing the lowest substrate temperatures during growth compared to other techniques, is the most suitable method to provide good quality GaInAsSb alloys even into the miscibility gap [9], which is necessary to extend the wavelength beyond 2.47 μm.

Thus far, GaInAsSb detectors have been studied using the front-illuminated (F-I) configuration. Of late, the demand for focal plane arrays of these sensors has been increasing rapidly and so has the number of pixels in each array [10]. As the size of the array increases, flip-chip bonding becomes necessary due to the sheer number of pixels that require an individual connection. Flip-chip packages offer a number of additional advantages over the widely used wire-bonding technique, including high I/O density and short interconnect distance between the chip and the substrate leading to high device performance, miniature devices and excellent heat dissipation. For flip-chip mounting, back-illumination is the most favoured configuration. Therefore, we undertake here to study GaInAsSb detectors under back-illumination (B-I) and compare their performance with front-illumination (F-I) devices at room temperature. To the best of our knowledge, no comparative study between these two configurations has been previously undertaken. In order to keep the comparison meaningful, these structures were grown and fabricated under identical conditions. In this paper, we describe MBE growth, processing and characterization of

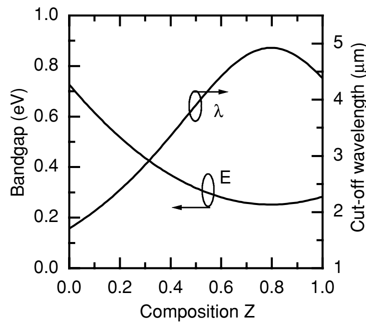

Figure 1. Room temperature variation of the bandgap of a $Ga_xIn_{1-x}As_ySb_{1-y}$ quaternary alloy, which stays lattice matched to GaSb so long as the elemental concentrations are in the ratio $(InAs_{0.91}Sb_{0.09})_z(GaSb)_{1-z}$, as a function of z ($x = 1 - z$, $y = 0.91z$). The plot is based on equations provided in [11].

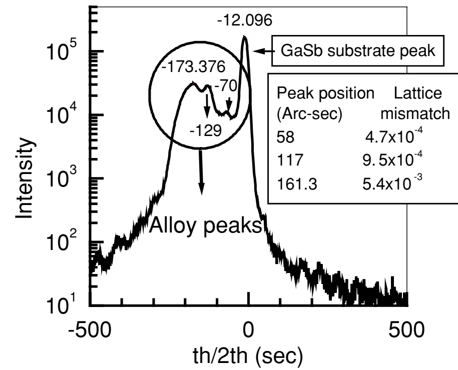

Figure 2. Fine tuning of the lattice constant of a quaternary $Ga_{0.79}In_{0.21}As_ySb_{1-y}$ alloy (ia1167) to the GaSb substrate lattice constant by making small variations in y. In this case, variation of $J_{As}/(J_{As} + J_{Sb})$ was achieved by varying the Sb flux J_{Sb} in three consecutive half micron quaternary alloy layers while holding x and As flux constant, followed by post-growth measurement and analysis of high-resolution x-ray diffraction rocking curves. The inset shows the diffraction peak position of each quaternary alloy layer relative to the GaSb diffraction peak, along with the corresponding lattice mismatch of the quaternary alloy to the GaSb substrate.

GaInAsSb detectors, specifically comparing and contrasting B-I and F-I devices.

2. Experimental details

2.1. MBE growth

A solid-state molecular beam epitaxy system was used for the growth of the device structures. Dual filament Sumo cells were used for the group III sources and valved cracker cells for the group V sources. Be and GaTe were used as p and n dopants, respectively. The substrate temperature during the growth was measured using an optical pyrometer. The substrates were slowly heated to approximately 510 °C under a Sb flux to desorb the oxide. Subsequently, the substrate temperature was brought down to 490 °C for the growth of a doped GaSb buffer layer. All the subsequent layers were grown around 460 °C.

The values of the x and y concentrations of the $Ga_xIn_{1-x}As_y Sb_{1-y}$ are uniquely determined by both the desired bandgap of the quaternary alloy and the requirement of lattice matching to a GaSb substrate. For example, as illustrated in figure 1, the quaternary alloy with a ratio of elemental components $(InAs_{0.91}Sb_{0.09})_z(GaSb)_{1-z}$ (so $x = 1 - z$, $y = 0.91z$) stays lattice matched to GaSb with a range of useful bandgaps on the high energy side from 0.727 to 0.594 eV (1.7–2.5 μm) at room temperature as z varies from 0 to about 0.23 (depending on the growth technique) before the alloy miscibility gap is entered [11].

The group III fluxes required to achieve a desired x concentration of the $Ga_xIn_{1-x}As_y Sb_{1-y}$ alloy were determined simply from the growth rates of GaSb and InAs on a GaSb substrate. At the substrate temperatures employed during this growth (450–490 °C), the group III elements have a sticking coefficient of approximately unity and thus their concentration x is determined simply from the appropriate ratio of growth rates [12] $x = R_{GaSb}/R_{Tot}$, with $R_{Tot} = R_{GaSb} + R_{InAs}$. The growth rates of GaSb (R_{GaSb}) and InAs (R_{InAs}) on GaSb have an exponential dependence on the group III cell temperature alone and are independent of group V flux. Initially, R_{GaSb} and R_{InAs} were calibrated against cell temperature using reflection high-energy electron diffraction (RHEED) intensity oscillations under excess group V flux. Cell temperatures/growth rates were then chosen to obtain the desired x concentration. Total growth rate for the structures reported here was 0.703 monolayers s^{-1}.

Finding the correct group V fluxes, J_{Sb} and J_{As}, to achieve the desired y of the $Ga_xIn_{1-x}As_y Sb_{1-y}$ alloy is not as straightforward as the group III case, because neither of the V elements has unity sticking coefficient, and the competition between the V elements for incorporation into the alloy is not straightforward. First, group V fluxes were calibrated by measuring the beam equivalent pressure (BEP) as a function of V-cell valve position. The total V/III flux ratio in the growth of the structures here was kept just above stoichiometric conditions, about 3. The precise $J_{As}/(J_{Sb} + J_{As})$ flux ratio to achieve the desired y for lattice matching was determined by some trial and error. Because x of the alloy is set as described above, the desired y of the alloy of target bandgap is achieved automatically when the alloy is lattice matched to GaSb. The degree of lattice mismatch of the alloy to GaSb can be determined directly by a post-growth measurement with high resolution x-ray diffraction (HRXRD).

For example, figure 2 shows the high resolution x-ray diffraction (HR-XRD) spectra of a sample (ia1167) grown with three consecutive half micron layers of $Ga_xIn_{1-x}As_y Sb_{1-y}$ alloy, each with fixed x (= 0.79) but with three variations of y, which is varied by changing the $J_{As}/(J_{Sb}+J_{As})$ flux ratio. Each value of y in turn gives rise to an alloy with a different lattice constant and with a distinct XRD peak. The lattice mismatch of the alloy compared to GaSb is equal to the separation of the alloy and GaSb diffraction peaks times the conversion factor 8.3×10^{-6} $arcs^{-1}$, as determined by the Bragg condition. The leftmost XRD peak in figure 2 is the alloy that resulted from an initial estimate of the $J_{As}/(J_{Sb} + J_{As})$ ratio of fluxes based on the y concentration of As. As the y concentration is increased (by decreasing the Sb flux in this case; the lattice constant can also be varied by changing the As flux [13]), the quaternary peak shifts further towards the substrate peak. The V-flux ratio versus lattice constant data, derived from figure 2, can be extrapolated to achieve fine tuning of the

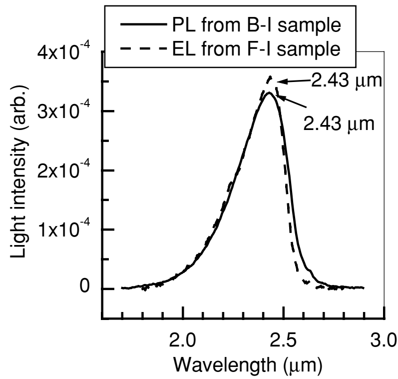

Figure 3. Room temperature electroluminescence spectrum of the F-I sample (ia1185) and the photoluminescence spectrum of a $Ga_xIn_{1-x}As_ySb_{1-y}$ quaternary alloy calibration sample (ia1208) grown before the B-I sample (ia1209). Both samples are lattice matched to GaSb, so alloy compositions, determined uniquely from the plot in figure 1, are $x = 0.79$ and $y = 0.19$.

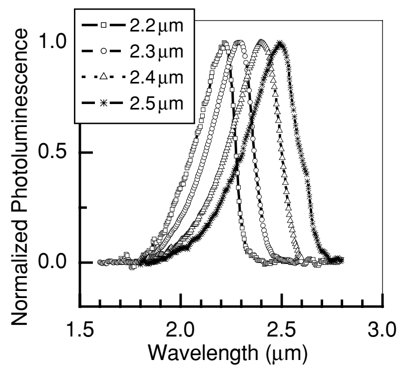

Figure 4. Bright room-temperature photoluminescence was achieved for $(InAs_{0.91}Sb_{0.09})_z(GaSb)_{1-z}$ epi-layers lattice matched to the GaSb substrate with bandgaps varying from 2.2 μm to 2.5 μm, corresponding to z's from 0.15 to 0.23 as determined by the plot in figure 1.

lattice constant. Using this technique, samples used in this study for the fabrication of detectors had a lattice mismatch less than $\pm 5 \times 10^{-4}$.

The composition of the quaternary was cross checked by determining the energy bandgap from a room temperature photoluminescence (PL) measurement, which can be determined directly from figure 1 if the alloy is lattice matched to GaSb. Room temperature electroluminescence from the F-I sample and PL from a calibration sample (ia1208) grown just before the growth of the B-I sample and lattice matched to GaSb showed the emission peaks at the same wavelength, i.e., 2.43 μm (figure 3). Figure 1 shows that the composition of the alloy in both cases is $Ga_{0.79}In_{0.21}As_{0.19}Sb_{0.81}$.

Figure 4 shows the normalized room-temperature PL from GaInAsSb samples lattice matched to GaSb with peak PL extending across the wavelength region of interest, 2.0–2.5 μm. Figure 1 gives the element ratios of the lattice matched quaternary $(InAs_{0.91}Sb_{0.09})_z(GaSb)_{1-z}$ corresponding to z's of about 0.15 to 0.23.

2.2. Detector design

B-I and F-I detectors consisted of a $Ga_{0.79}In_{0.21}As_{0.19}Sb_{0.81}$ quaternary p–i–n homojunction photodiode grown on doped (1 0 0)-oriented GaSb substrates about 500 μm thick. P–i–n detectors operate by generation of a current of electrons and holes from the absorption of incident light in the 'i-region'. The electrons and holes are accelerated to the n and p regions, respectively, where they are collected by the metal contacts.

The detailed layer structures used for B-I and F-I configuration detectors are shown in figure 5 (samples ia1209 and ia1185, respectively). For the B-I detector, light illumination occurred through the 'backside' or n-GaSb substrate. N-rather than p-GaSb substrates were used for the B-I case to avoid excess optical loss as light passed through the substrate. For example, a 500 μm n-GaSb substrate doped to about 5×10^{17} cm^{-3} showed negligible optical loss

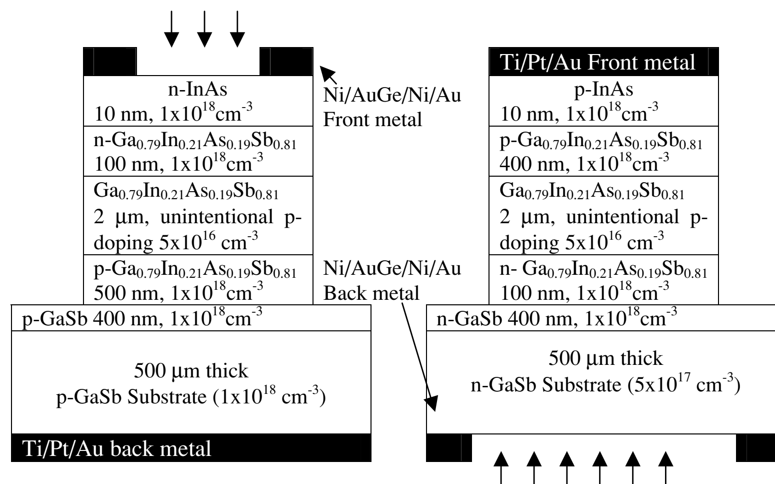

Figure 5. Device structure of the front-illumination (left) and back-illumination (right) detectors. The F-I detector has a circular mesa with a diameter of 410 μm and a circular active area with a 200 μm diameter. The back-illuminated device is a circular mesa with a 125 μm diameter.

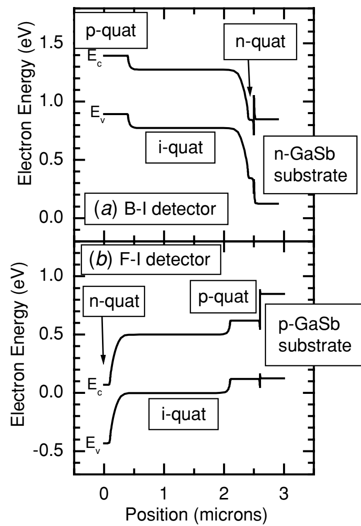

Figure 6. Real space energy band diagram of the (*a*) B-I detector structure and (*b*) F-I detector structure. For the B-I detector, photogenerated electrons encounter a heterointerface at the n-$Ga_{0.79}In_{0.21}As_{0.19}Sb_{0.81}$/n-GaSb junction. Heavy n-doping of the two layers aligns the conduction bands and creates only a low, narrow Schottky barrier. For the F-I detector, holes encounter the heterointerface. Again, heavy doping of both layers aligns the bands and creates only a low, narrow Schottky barrier.

(absorption coefficient *x* substrate thickness, $\alpha L < 0.1$) over the wavelengths of interest (2.0–2.5 μm) as compared to those of 500 μm thick p-GaSb substrates doped to about 1×10^{18} cm^{-3}, which showed a very high optical loss ($1.8 < \alpha L < 3.0$) in the same wavelength region due to higher free-carrier absorption.

The real space band diagram of the B-I p–i–n detector on n-GaSb, shown in figure 6(*a*), shows that electrons collected from the i-region encounter a heterointerface between the n-$Ga_{0.79}In_{0.21}As_{0.19}Sb_{0.81}$ and the n-GaSb substrates. The conduction bands for the two regions align due to the heavy doping of each layer, and only a very low, thin Schottky barrier results which does not impede collection of electrons.

For the F-I detector, on the other hand, a p-GaSb substrate was used, so that light, incident on the detector from the front or epi-layer side, would pass through a thin n-doped quaternary region rather than a lossy p$^+$-doped GaInAsSb layer en route to the i-region. The real space band diagram of the F-I p–i–n detector in figure 6(*b*) shows that in this case it is the holes that encounter the heterointerface between the p-$Ga_{0.79}In_{0.21}As_{0.19}Sb_{0.81}$ and the p-GaSb substrates. Again, heavy doping of both layers aligns the valence bands, and only a low, thin Schottky barrier results which does not impede the collection of holes.

For both B-I and F-I detectors, the i-region consists of a 2 μm thick $Ga_{0.79}In_{0.21}As_{0.19}Sb_{0.81}$ layer, thick enough to absorb light above the cut-off wavelength with high efficiency, but thin enough to allow electrons and holes to reach the n and p regions before recombining. The 'i-region' actually had an unintentionally p-doping level of about 5×10^{16} cm^{-3}, as determined by separate room temperature Hall measurements of the quaternary grown on GaAs substrates, typical of antimonide semiconductor alloys due to the formation of native defects.

2.3. Device processing

Device processing was started with a photolithography step to define ring contacts of 400 μm outer diameter and 200 μm inner diameter on the F-I sample, as shown in figure 5. Ni/AuGe/Ni/Au metals were deposited on the top, n-side of the F-I sample. The metal was lifted off selectively on the F-I sample to leave the ring metal contacts intact. A second lithography step was carried out on the F-I sample to define circular mesas of 410 μm diameter enclosing the ring contacts. First, a 120 nm thick SrF_2 layer was deposited on both the samples as a dry etch mask, followed by a lift-off step to selectively leave only the contacts covered by SrF_2. Next, reactive ion etching was used to etch the mesas down to the bottom heavily-doped GaSb epitaxial layer using a mixture of BCl_3 and Cl_2. Subsequently, Ti/Pt/Au was deposited as a metal contact on the back, p-side of the F-I sample.

For the B-I detector, the same steps were followed, except Ti/Pt/Au was deposited on the top as a solid circle rather than a ring contact, and mesas were only 125 μm in diameter. A shadow mask was used on the backside to deposit Ni/AuGe/Ni/Au around the edge of wafer, leaving most of the backside available for illumination.

2.4. Device characterization

The responsivity measurements of the GaInAsSb p–i–n detectors were performed at room temperature with a Nicolet FTIR-Magna 56 spectrometer attached to a microscope. The responsivity of each detector mesa was spectrally resolved from 1.5 to 3.0 μm with an instrument bandpass of 2.5 nm. The responsivity of the detector was determined by normalizing the measured spectrum with that of a commercial InAs detector. The *I–V* measurements of the detectors were performed using a Hewlett Packard 4155A semiconductor parameter analyser.

3. Results and discussion

In the following discussion, both the F-I and B-I detectors are analysed in terms of the zero bias dynamic resistance, defined as $(R_0 = \mathrm{d}I/\mathrm{d}V)^{-1}{}_{V=0}$—mesa area ($A$) product R_0A; and the spectral responsivity R_λ defined as the Amps of current generated by the detector at zero bias voltage per watt of incident light. Together, these two important figures of merit characterize the D^* of the detector, which is a measure of the S/N of the detector per unit incident radiation: $D^*(\lambda) = R_\lambda(R_0A/4k_BT)^{1/2}$, where k_B is the Boltzman constant and T is the temperature.

Figure 7 shows the dark *I–V*, and the product of dynamic resistance $R = (\mathrm{d}I/\mathrm{d}V)^{-1}$ and device area A plotted against the applied bias of some of the best detectors on the F-I and B-I samples. The diodes show low forward dynamic resistance indicating the good quality of the contacts and low series resistance in both types of detectors. The product RA increases linearly up to a reverse bias of 0.08 V ($\sim 3kT/q$) and thereafter remains more or less constant. Such a rise in RA has also been observed by others [14] along with a sharp reduction upon further increasing the reverse bias. The initial rise in RA is due to the gradual reduction of diffusion current to a steady-state value, and the sharp reduction has been attributed to the onset of tunnel dark current. In this case, it can be concluded that the

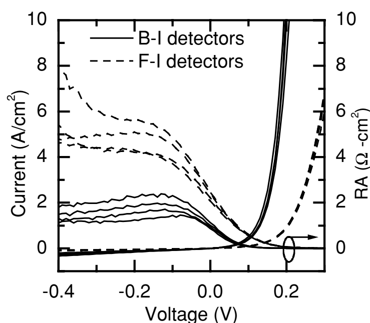

Figure 7. Current density and differential resistance-area product of F-I and B-I detectors versus voltage at room temperature. *RA* reaches a maximum value of 5 and 2 Ω cm^2 respectively at a reverse bias of 80 mV and then remains more or less constant with further increase in reverse bias. The zero bias resistance area product R_0A, which is a figure of merit that affects the detector performance, is 1 and 2.2 Ω cm^2 for F-I and B-I samples respectively.

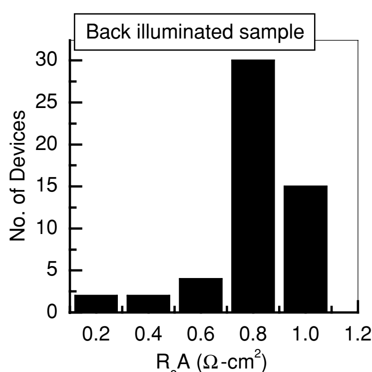

Figure 8. The bar chart showing the variation of R_0A across the B-I detector array. The array shows a small spread with a mean of 0.8 Ω cm^2 and a low standard deviation of 0.18 Ω cm^2.

contribution of the tunnelling component in the reverse bias dark current is small.

In figure 7, it can be seen that the average R_0A for the B-I and F-I detectors are 1 and 2.2 Ω cm^2, respectively. A R_0A histogram of several B-I diodes shown in figure 8 demonstrates that the device process utilizing the mesa dry etch is capable of yielding a large array with excellent uniformity in device parameters. A separate experiment to study the dependence of R_0A on the device mesa size showed that the R_0A of the devices under study are limited by the current leakage at the side walls. Leakage currents limit R_0A to a greater degree in the B-I devices because they have a larger perimeter-to-area ratio than the F-I devices. We are currently looking into several passivation methods to eliminate side wall current leakage.

Figure 9 shows the spectral responsivity of some of the best F-I and B-I devices measured under zero bias voltage. For both the samples, the absorption edge starts at 2.6 μm, which matches with the observed PL long-wavelength fall-off. The responsivity spectrum of the B-I sample looks different in two respects. The responsivity falls sharply at the shorter wavelength side due to the GaSb substrate absorption edge. On the longer wavelength side, the responsivity rises sharply, reaching about 80% of the maximum value at 2.43 μm.

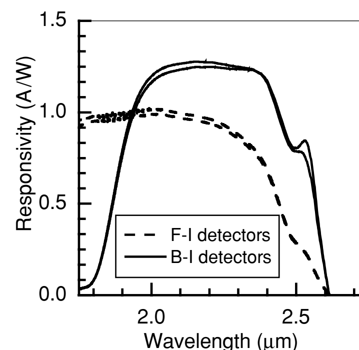

Figure 9. Current responsivity versus wavelength curves for F-I and B-I detectors. Measurements were performed under zero bias voltage at room temperature. For each of the device geometries, measurements are shown for two different mesa devices on the same sample wafer.

On the other hand, the F-I sample shows a more subdued increase in the response, reaching a value of only 50% at the energy 2.43 μm.

In figure 9, it can also be seen that the B-I detector has a larger and flatter response. It shows 90% of the maximum response over a range of 2–2.4 μm and a maximum responsivity of 1.19 A W^{-1} between 2.2 and 2.35 μm. This amounts to a quantum efficiency (η) of 65%. This value is amongst the largest reported at 2.35 μm [5] with no antireflection coating. On the other hand, the F-I sample shows a maximum response of 1 A W^{-1} (η = 62%) at 2.01 μm and 0.78 A W^{-1} (η = 41%) at 2.35 μm, and 95% of the maximum value for the wavelength range of 1.69–2.24 μm.

The larger responsivity shown by the B-I sample can be attributed to two main causes. First, in the B-I case, the back metal acts as a reflector for both the photons not absorbed in the active layer and for the photons resulting from radiative recombination, which would normally be absorbed in the p-substrate in the conventional F-I design. These reflected photons get reabsorbed in the active region, and this photon recycling contributes to the quantum efficiency. It has been reported earlier that the room-temperature PL and the time-resolved PL measurements show three times larger PL and twice as long a PL decay time for the samples with a reflector when compared to those without a reflector [15, 16]. These results show that the backside reflector improves collection efficiency, optical absorption and photon recycling.

Second, in the B-I case, most of the photons, at least those of shorter wavelength, get absorbed in the active layer near the active/substrate interface which results in reduced surface recombination. In a conventional F-I detector, the shorter wavelength photons are absorbed near the sample top surface where the recombination effects are prominent [17]. The other benefits of B-I devices are the 100% utilization of diode mesa area for the light absorption and carrier generation, and effective carrier collection across the whole diode area. The F-I devices have contacts that obstruct the incoming light: only one-fourth of the mesa area is useful, but all of it produces noise. In addition, the diffusion of carriers to the contact may be an issue for the ring contact in the F-I geometry.

Finally, we note that while n-InAs is a natural choice for a thin contact layer on the n-GaInAsSb of a F-I device due to the

low-energy conduction band of InAs compared to GaInAsSb ($\Delta(CB)_{InAs\text{-}Ga_{0.79}In_{0.21}As_{0.19}Sb_{0.81}} = -0.71$ eV [11]), p-InAs on p-GaInAsSb is not the ideal choice of a contact layer for a B-I device, where the low (electron) energy valence band of InAs compared to GaInAsSb ($\Delta(VB)_{InAs\text{-}Ga_{0.79}In_{0.21}As_{0.19}Sb_{0.81}} = -0.41$ eV[11]) could actually make the Schottky barrier at the metal contact higher. For this study, however, a doped InAs layer was used for both F-I and B-I devices to facilitate comparison. In future, however, a p-GaSb contact layer would be more ideal on the B-I structure.

In conclusion, we have shown GaInAsSb p–i–n detectors lattice matched to GaSb substrates and under back-illumination, a critical geometry for flip-chip focal plane arrays, give equal or superior performance from 2.0 to 2.5 μm compared to similar front-illuminated GaInAsSb p–i–n detectors. The back-illuminated detectors show larger quantum efficiency and a flatter response. This improved performance is attributed to an improved collection efficiency and photon recycling due to reflection from the back metal contact and reduced carrier recombination at the substrate/active interface. We have also described a method for the MBE deposition of high-quality lattice-matched GaInAsSb alloy on the GaSb substrate using RHEED intensity oscillations and post-growth XRD techniques.

Acknowledgments

The authors thank NIH for support for this work under contract no 1R01DK64569-01.

References

[1] Carter B L, Shaw E, Olesberg T, Chan W K, Hasenberg T C and Flatte M E 2000 *Electron. Lett.* **36** 1301–303
[2] Hamamatsu Photonics 2001 *InGaAs PIN Photodiodes* Cat. No. KIRDO003E01 (Japan)
[3] Plis E, Rotella P, Raghavan S, Dawson L R and Krishna S 2003 *Appl. Phys. Lett.* **82** 1658–60
[4] Krier A and Mayo Y 1997 *Infrared Phys. Technol.* **38** 397–403
[5] Andreev I A, Il'inskaya N D, Kunitsyna E V, Mikhaĭlova M P and Yakovlov Yu P 2003 *Semiconductors* **37** 949–54
[6] Cederberg J G, Hafich M J, Biefeld R M and Palmisiano M 2003 *J. Cryst. Growth* **248** 289–95
[7] Wang C A, Choi H K and Charache G W 2000 *IEE Proc.-Optoelectron.* **147** 193–8
[8] Zhang X, Li A Z, Lin C, Zheng Y L, Xu G Y, Qi M and Zhang Y G 2003 *J. Cryst. Growth* **251** 782–6
[9] Choi H K, Eglash S J and Turner G 1994 *Appl. Phys. Lett.* **64** 2474–6
[10] Jiang J, Tsao S, O'Sullivan T, Razeghi M and Brown G J 2004 *Infrared Phys. Technol.* **45** 143–51
[11] Vurgaftman I, Meyer J R and Ram-Mohan L R 2001 *J. Appl. Phys.* **89** 5815–75
[12] Eglash S J, Choi H K and Turner G W 1991 *J. Cryst. Growth* **111** 669–76
[13] Simanowski S, Walther M, Schmitz J, Kiefer R, Herres N, Fuchs F, Maier M, Mermelstein C, Wagner J and Wiemann G 1999 *J. Cryst. Growth* **201/202** 849–53
[14] Piotrowski T T *et al* 2000 *MRS Symp. Proc.* **607** 89–94
[15] Lee T P, Burrus C A, Dentai A G and Ogawa K 1980 *Electron. Lett.* **16** 155
[16] Wang C A *et al* 2004 *J. Electron. Mater.* **33** 213–17
[17] Borrego J M, Saroop S, Gutman R J, Charache G W, Donovan T, Baldasaro P F and Wang C A 2001 *J. Appl. Phys.* **89** 3753–9